Supplementary Information

Beyond Superexchange: Emergent Unconventional Ferromagnetism in Thin-Film Sandwich Structures of Intrinsic Magnetic Topological Insulators

Takuya Takashiro[1*†], Ryota Akiyama[1‡], Ryotaro Minakawa[1], and Shuji Hasegawa[1]

[1]*Department of Physics, The University of Tokyo, Bunkyo, Tokyo 113-0033, Japan*

Corresponding author: [†] takuya.takashiro@jku.at (T.T.),

[‡] akiyama@surface.phys.s.u-tokyo.ac.jp (R.A.)

---

[*]*Present address: Institute of Semiconductor and Solid State Physics, Johannes Kepler University, Linz, 4040, Austria*

I. Thin film fabrication

All thin films were prepared by molecular beam epitaxy (MBE) in an ultrahigh vacuum chamber of ~1×10^{-10} Torr, equipped with a reflection high-energy electron diffraction (RHEED) system. After preparing a clean Si(111)-7×7 surface on a *n*-type middle-doped substrate by cycles of resistive heat treatment, a *N* quintuple layer (QL) thick $(Bi_{1-x}Sb_x)_2Te_3$ (BST) film was grown with co-evaporation of Bi and Sb on the substrate at ~200°C under Te-rich condition. As for Sb_2Te_3, we prepared the Si(111)-$\sqrt{3}\times\sqrt{3}$-Bi surface in advance because the high-quality epitaxial film was not obtained on Si(111)-7×7 surface due to the higher interface free energy between Sb_2Te_3 and Si(111). Then, we grew one septuple layer (SL) thick $Mn(Bi_{1-x}Sb_x)_2Te_4$ (MBST) film on *N*-1 QL BST by depositing Mn on *N* QL BST at ~270℃ under Te-rich condition. By such procedures, we fabricated MBST/BST heterostructures and MBST/BST/MBST sandwich structures [1,2]. Figure S1 shows the RHEED patterns after the growth of MBST on BST. The sharp streaky MBST 1×1 pattern indicates that an atomically flat and single crystalline epitaxial MBST/BST film was grown in [001] crystallographic orientation (*c*-axis) of the hexagonal unit cell. In order to avoid oxidation after the growth, we deposited Al on top at room temperature to form a ~2-nm-thick Al_2O_3 cap layer when it was taken out in air for *ex situ* measurements.

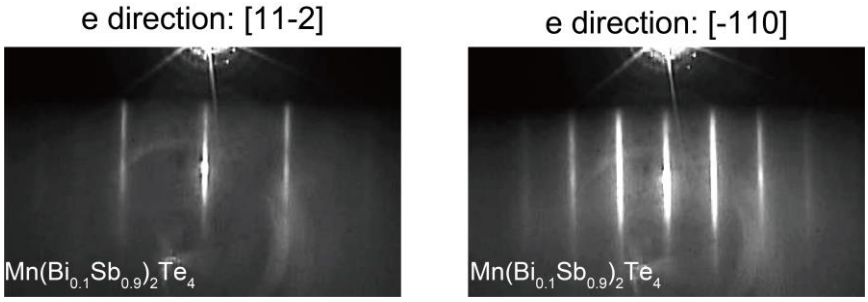

Fig. S1 RHEED patterns of as-grown MBST/BST observed from [11-2] (left) and [-110] (right) incidence of the Si(111) substrate, respectively.

II. Out-of-plane and in-plane lattice constants obtained by the XRD measurements

As described in the main text, all thin films that consist of BST and MBST are epitaxially grown in their [001] crystallographic orientation (c-axis) of the hexagonal unit cell on Si(111) as shown in Fig. S2(a). In our XRD measurements, the 2θ-θ scans with respect to (001) and (015) planes were performed to estimate the out-of-plane (c) and in-plane lattice constants (a, b). In a hexagonal lattice, where $|\mathbf{a}| = |\mathbf{b}| = a$ and $|\mathbf{c}| = c$ are different from each other and the angle between the a(b)- and c-axes is 90° while that between the a- and b-axes is 120°, the relation between the (hkl) plane distance (d_{hkl}) and the reciprocal vector (**G**), $|\mathbf{G}| = 1/d_{hkl}$, is deformed to $1/d_{hkl}^2 = 4(h^2 + hk + k^2)/2a^2 + l^2/c^2$. Thus, when we measure the 015 peak position containing the information of both a and c-axes described by $1/d_{015}^2 = 4/3a^2 + 25/c^2$ in addition to measuring the 00l peak position containing the information of c-axis only, we can obtain in-plane lattice constants as well as out-of-plane

lattice constants. In the case of $MnBi_2Te_4/Bi_2Te_3$, a = 4.37 Å is estimated by observing both 0015 (l = 15) and 015 diffraction peaks and using the above formula. These obtained values are comparable with the previously reported in-plane lattice constants of Bi_2Te_3 and $MnBi_2Te_4$ [3,4]. Figures S2(b,c) show the x-dependences of the out-of-plane lattice constant (c) and d-spacing of the (015) plane of the MBST/BST heterostructures. Both were used to obtain the x-dependence of a in Fig. 2 in the main text.

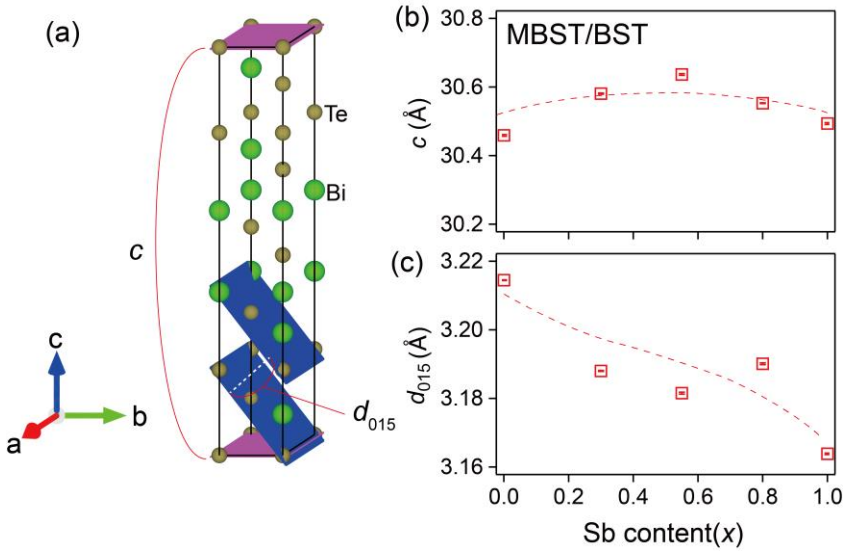

Fig. S2 (a) Schematic of a unit cell of the hexagonal lattice of the Bi_2Te_3 crystal. c and d_{015} correspond to the (001) and (015) plane distances, respectively. (b,c) x-dependences of (b) c and (c) d-spacing of (015) plane values in MBST/BST.

III. Transport properties of MBST/BST

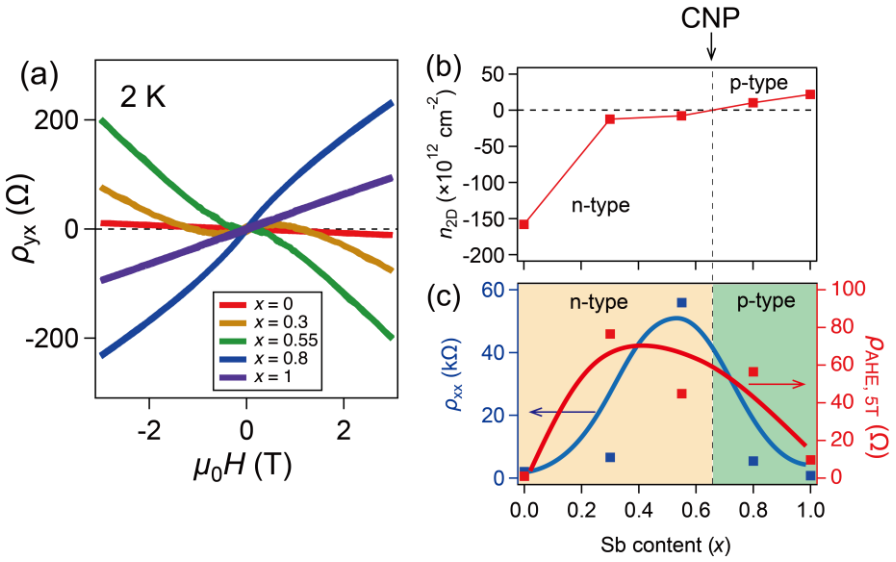

Fig. S3 Electrical transport measurements in MBST(1 SL)/BST(8 QL) with various Sb contents, x. (a) Magnetic field dependences of Hall resistivity (ρ_{yx}) at x = 0, 0.3, 0.55, 0.8, and 1. (b) x-dependence of 2D carrier type/density (n_{2D}) at T = 2 K. As x increases, the carrier type is changed from n to p-type around x = 0.55-0.8. (c) x-dependences of longitudinal resistivity (ρ_{xx}) and anomalous Hall resistivity at 5 T ($\rho_{AHE,5T}$) at T = 2 K. The blue and red plots indicate ρ_{xx} and $\rho_{AHE,5T}$, respectively. Both curves serve as guides for the eyes.

Figure S3(a) shows the magnetic field dependence of the Hall resistivity (ρ_{yx}) of the MBST/BST heterostructure with various Sb contents x (x = 0, 0.3, 0.55, 0.8, and 1). The nonlinear behavior of these curves at low magnetic fields indicates the existence of the anomalous Hall effect (AHE). From the slope of ρ_{yx} at high magnetic fields (corresponding to the component of the ordinary Hall effect), the carrier type and density n_{2D} are estimated as shown Fig. S3(b). The number of carrier electrons decreases as x increases, and the carrier type switches from n to p-types around x = 0.55 – 0.8, which

indicates that the Fermi level (E_F) approaches to the charge neutral point (CNP). On the other hand, the anomalous Hall resistivity is obtained after the subtraction of the ordinary Hall component from ρ_{yx}. Figure S3(c) displays x-dependences of the longitudinal resistivity (ρ_{xx}) and anomalous Hall resistivity at $\mu_0 H = 5$ T ($\rho_{AHE,5T}$) at $T = 2$ K indicated by the blue and red plots, respectively. ρ_{xx} becomes larger as x is closer to the Sb-content corresponding to CNP, which suggests that the heterostructure becomes more insulating as E_F approaches to CNP. As well as ρ_{xx}, $\rho_{AHE,5T}$ tends to be enhanced by positioning E_F closer to CNP. In general, the anomalous Hall resistivity is described by a product of the anomalous Hall coefficient (R_{AH}) and the magnetization (M). If the intrinsic scattering between carriers and local magnetic moments is assumed in a ferromagnetic topological insulator (FMTI), R_{AH} is dependent on its Berry curvature in k-space and thus enhanced as E_F is tuned near CNP [1, 5,6,7,8]. Therefore, the x-dependence of $\rho_{AHE,5T}$ in the present work illustrates the existence of the intrinsic AHE. One can note that in the MBST/BST/MBST sandwich structure, the x-dependence of the anomalous Hall resistivity represents the same tendency as the MBST/BST case because of such intrinsic AHE [1].

IV. Saturated magnetization of MBST/BST

Table S1 The saturated magnetization (M_{sat}) of MBST(1-SL thick)/BST heterostructures with various Sb-contents (x) at 2 K. These values of magnetization are normalized per one Mn atom at each sample, which is estimated to be the magnetic moment of a Mn^{2+} ion having 5 μ_B.

	x = 0	x = 0.3	x = 0.55	x = 0.8	x = 1
M_{sat} (μ_B/Mn)	5.1	4.8	5.9	4.3	5.2

Table S1 exhibits the saturated magnetization (M_{sat}) of MBST(1-SL thick)/BST heterostructures with various Sb-contents (x) at 2 K, which is derived from *M-H* curves at high magnetic fields (40 – 50 kOe). The saturated magnetization is normalized as the averaged magnetic moment of one Mn atom in each sample. It is shown that values of the saturated magnetization among all samples are within 4 ~ 6 μ_B/Mn, which corresponds to the magnetic moment ~ 5μ_B expected for Mn^{2+} ions. This result implies that all spins of Mn in our systems including one SL can be easily ordered in parallel when a high magnetic field is applied. On the other hand, saturated magnetic moments of 7 SL-$MnBi_2Te_4$ and bulk-$MnSb_2Te_4$ are ~ 1.14μ_B/Mn [8] and ~ 1.98μ_B/Mn [9], respectively, and both of which are much smaller than those of the present MBST/BST. In the previously reported systems, the magnitude of the magnetic order can be modulated by the interlayer interaction between SL-SL or Mn^{Sb} anti-site defects, and may be more

complicated than that of our systems. In other words, it is possible that in our MBST/BST heterostructures, the ferromagnetism is hardly influenced by such interlayer interaction or anti-site defect.

V. Magnetic anisotropy of $MnBi_2Te_4/Bi_2Te_3/MnBi_2Te_4$ sandwich structure

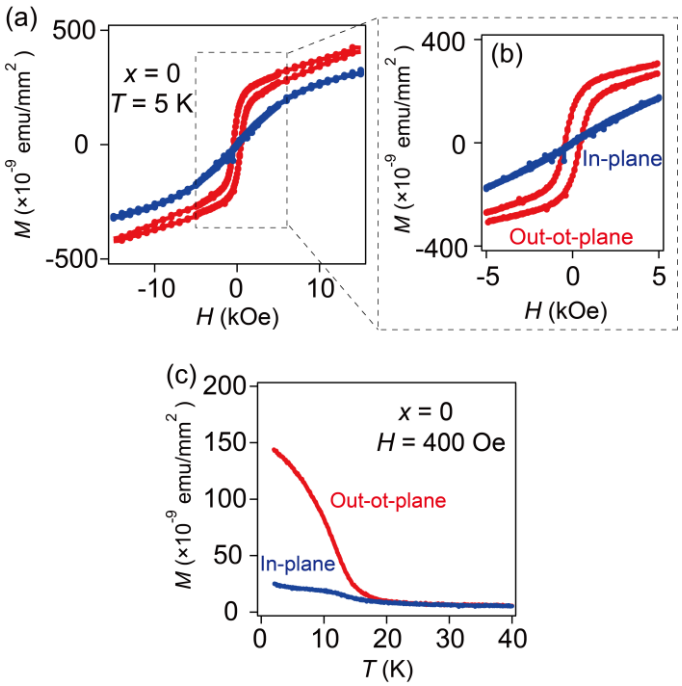

Fig. S4 Magnetic properties of $MnBi_2Te_4/Bi_2Te_3/MnBi_2Te_4$ sandwich structure under the magnetic field in the parallel (in-plane) and perpendicular (out-of-plane) directions to the sample surface. (a) In-plane (blue) and out-of-plane (red) *M*-*H* curves at $T = 5$ K. (b) Enlarged image of (a). (c) In-plane (blue) and out-of-plane (red) *M*-*T* curves under $H = 400$ Oe.

Figure S4 shows magnetic properties of the $MnBi_2Te_4/Bi_2Te_3/MnBi_2Te_4$ sandwich structure under external magnetic fields parallel (in-plane) and perpendicular (out-of-

plane) to the thin film plane. As shown in Figure S4(a,b), the *M-H* hysteresis of the out-of-plane case is much clearer and larger than that of the in-plane case. In addition, the comparison between the in-plane and out-of-plane *M-T* curves (Figure S4(c)) displays that the out-of-plane magnetization at $T = 2$ K is ~ 6 times as large as that of the in-plane case. These results illustrate that the out-of-plane direction of the sandwich structure sample is an easy-axis of the magnetization compared to the in-plane direction.

VI. Coercivity of MBST/BST/MBST sandwich structure

Figures S5(a) - (d) show *M-H* curves of MBST/BST/MBST sandwich structures with various x (0, 0.2, 0.7, and 1, respectively) at 2 K. Figure S5(e) shows x-dependences of coercivity H_C of the sandwich structures obtained in anomalous Hall effect (red) and SQUID (blue) measurements. The shape of *M-H* curves in Figs. S5(a) - (d), shows clear ferromagnetic hysteresis, and especially H_C decreases monotonically with increasing x; H_C: 1.3 $\rightarrow$ 0.2 kOe when x: 0 $\rightarrow$ 1 as seen by the blue plots in Fig. S5(e). As displayed in Fig. S5(e) and our previous study [1], the magnitude of H_C in anomalous Hall effect measurements also changes with x, but does not match the behavior in SQUID measurements, particularly when the Fermi level (E_F) is close to CNP ($x = 0.55$). This is because Hall components due to skyrmions are superimposed on the AHE signal if E_F is

closer to CNP, which leads to the difference in coercive forces between AHE and *M-H* curves.

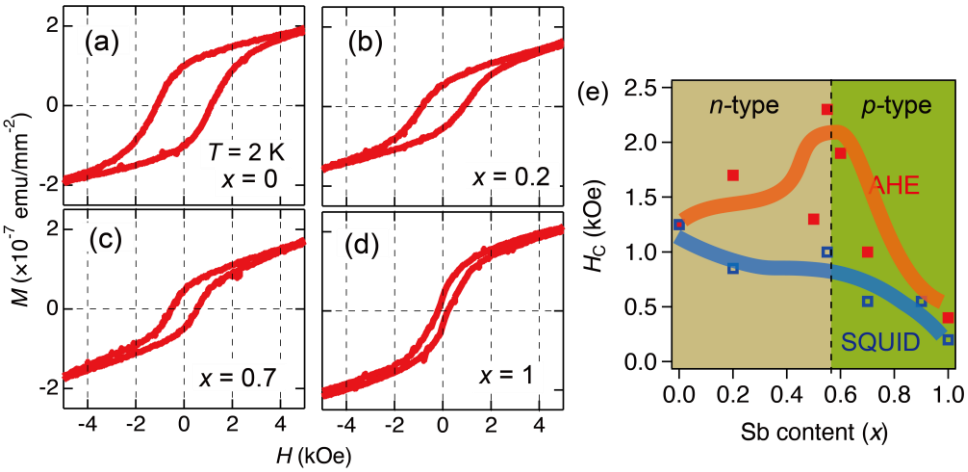

Fig. S5 (a-d) *M-H* curves of the MBST/BST/MBST sandwich structures with various *x* at 2 K by SQUID measurements. The applied magnetic field is perpendicular to the sample surface. (e) *x*-dependence of coercivity H_C of the MBST/BST/MBST sandwich structure at 2 K. The values obtained from anomalous Hall effect (AHE) and *M-H* (SQUID) measurements are shown as red and blue plots, respectively.

VII. Comparison of magnetic properties between the MBST/BST heterostructure and MBST/BST/MBST sandwich structure with Sb-contents (x = 0.55)

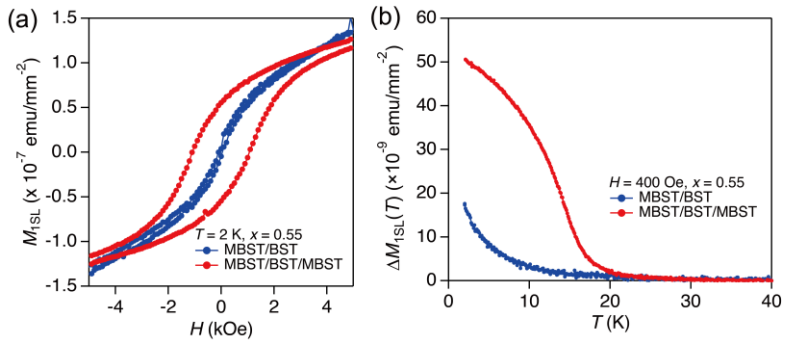

Fig. S6 (a) *M-H* curves under the normal-to-film magnetic fields in MBST/BST (blue) and MBST/BST/MBST (red) (x = 0.55) at 2 K. M_{1SL} indicates the normalized magnetization per a septuple layer of $MnBi_2Te_4$. (b) *M-T* curves under the normal-to-film magnetic fields in MBST/BST (blue) and MBST/BST/MBST (red) (x = 0.55) under H = 400 Oe. ΔM_{1SL} represents M_{1SL}(40 K) - $M_{1SL}(T)$.

Figures S6 (a) and (b) display *M-H* curves at T = 2 K and *M-T* curves under the magnetic field of H = 400 Oe, respectively. Here, the blue and red curves indicate the magnetic properties of the MBST/BST heterostructure and MBST/BST/MBST sandwich structure, respectively. The magnetization is normalized for a single septuple layer of MBST for comparison. As with the case without Sb-contents as exhibited in Fig. 3 in the main text, both the remanent magnetization and coercivity of the sandwich structure are much larger than those of the heterostructure. Thus, the interlayer magnetic interaction in the sandwich structure is still ferromagnetic even when Sb is substituted for Bi.

VIII. Arrott plots of sandwich structures

Figure S7 and S8 show *M-H* and corresponding Arrott plot curves of $MnBi_2Te_4/Bi_2Te_3/MnBi_2Te_4$ sandwich structures with various spacer thicknesses (0, 2, 6, and 9 QL) and MBST/BST/MBST with various Sb-contents (x = 0, 0.2, 0.55, and 1), respectively. From these results, the x- and spacer-thickness-dependences of T_C were obtained as illustrated in the main text.

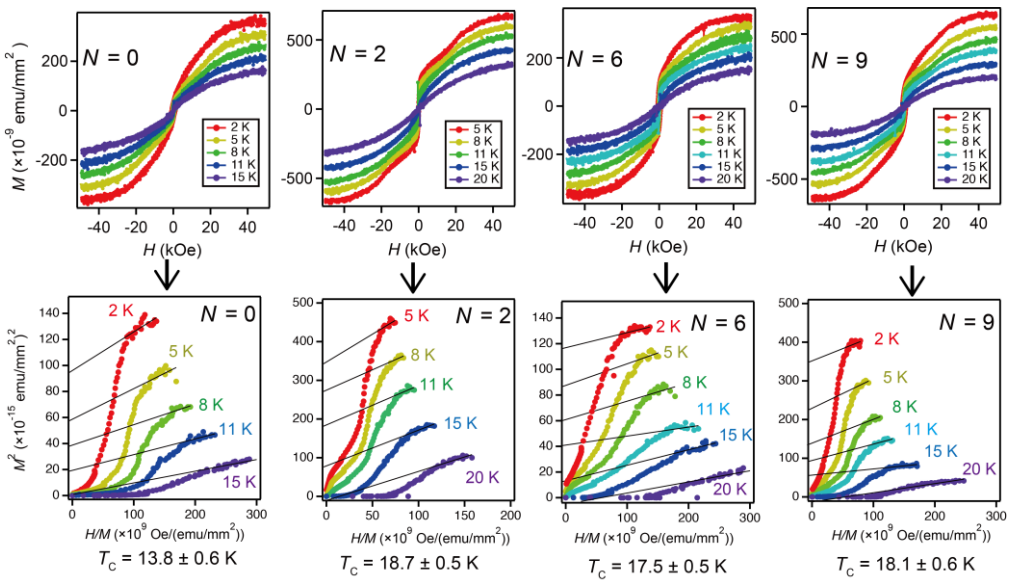

Fig. S7 (top) *M-H* curves of $MnBi_2Te_4/Bi_2Te_3$(*N* QL)/$MnBi_2Te_4$ sandwich structure with spacer thickness *N* = 0, 2, 6, and 9 measured at various temperatures, and (bottom) corresponding Arrott plot curves. The applied magnetic field is perpendicular to the sample plane.

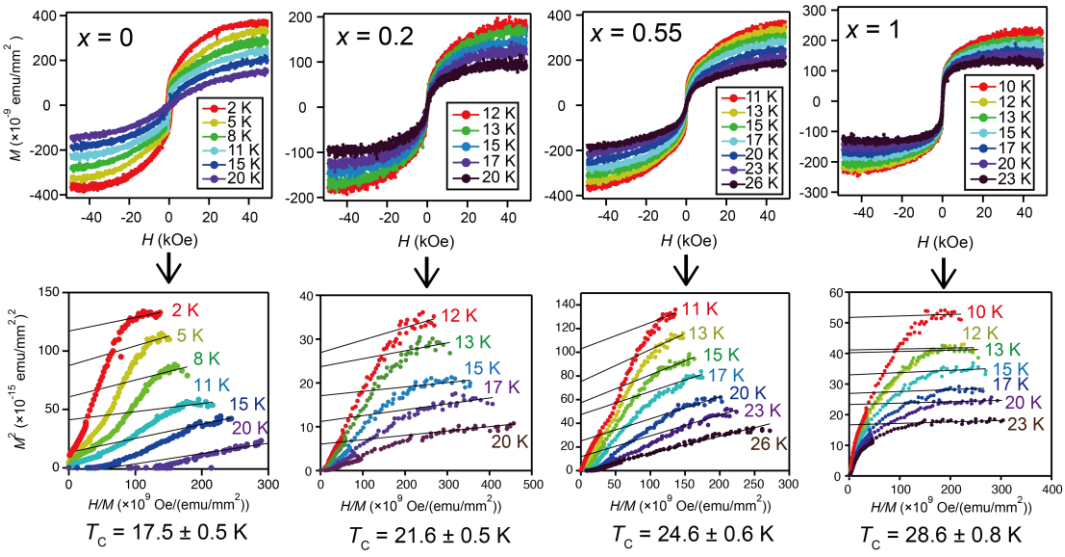

Fig. S8 (top) *M-H* curves of MBST/BST/MBST sandwich structures with *x* = 0, 0.2, 0.55 and 1 at various temperatures, and (bottom) corresponding Arrott plot curves. The applied magnetic field is perpendicular to the sample plane.

IX. Anomalous Hall effect modulated by ion-liquid gating

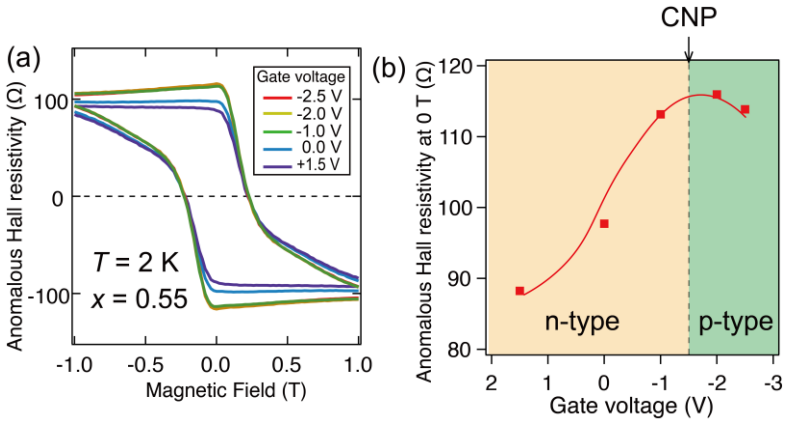

Fig. S9 (a) Magnetic field dependences of the anomalous Hall effect of the MBST/BST/MBST sandwich structure (x = 0.55) at 2 K with different gate voltages. (b) Gate-voltage dependence of the anomalous Hall resistivity at 0 T obtained from (a).

Figure S9(a) displays magnetic field dependences of anomalous Hall resistivity of the MBST/BST/MBST sandwich structure (x = 0.55) at T = 2 K with various gate voltages, derived from ρ_{yx} shown in Fig. 8 in the main text. Figure S9(b) shows the gate-voltage dependence of the anomalous Hall resistivity under 0 T (ρ_{AHE}) obtained from Fig. S8(a). The magnitude of ρ_{AHE} shows a maximum when the gate voltage approaches -2.0 to -1.0 V, specifically at CNP. In other words, AHE is enhanced as E_F is closer to CNP, which indicates that there is intrinsic AHE induced by the Berry curvature as mentioned in Section III. On the other hand, the coercivity of this sandwich structure is scarcely dependent on the gate voltage (namely the E_F position) as seen in Fig. S9(a), as mentioned in the main text. We mention here that, similarly, the FMTI $Cr_y(Bi_xSb_{1-x})_2Te_3$ system also shows both intrinsic AHE and the E_F-independent coercivity [7].

X. Comparison of Magnetic properties between 2 SL and 3 SL $MnBi_2Te_4$

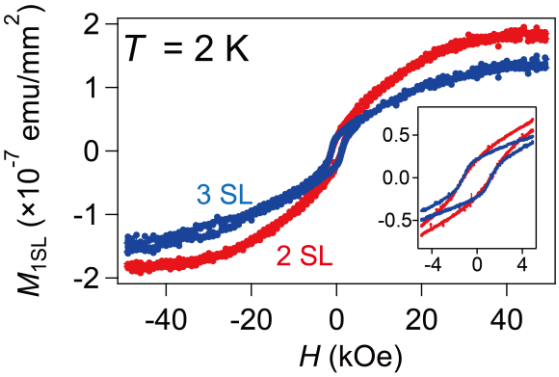

Fig. S10 *M-H* curves of 2 SL (red) and 3 SL (blue) thick $MnBi_2Te_4$ films at T = 2 K, respectively. Inset: Enlarged *M-H* curves at the low magnetic fields. M_{1SL} indicates the magnetization normalized per 1 SL (M_{1SL}.)

Figure S10 shows *M-H* curves of 2 SL and 3 SL thick $MnBi_2Te_4$ films grown on Si(111) substrates, in which each magnetization is normalized per 1 SL. As shown in the inset, the ferromagnetic hysteresis loop is observed in both samples. This illustrates that the interlayer interaction is ferromagnetic in the case of 3 SL as well as 2 SL stackings. On the other hand, the saturated net magnetization at H = 50 kOe of 3 SL sample is smaller than that of 2 SL sample. It has been reported that in multi-layered $MnBi_2Te_4$ systems such as bulk crystals, the antiferromagnetic properties are observed due to antiferromagnetic interlayer interaction [4,8,9]. Thus, it is possible that as the number of SLs increases, the ferromagnetic interlayer interaction becomes further smaller and is switched to the antiferromagnetic property at last.

References

[1] T. Takashiro, R. Akiyama, I. A. Kibirev, *et al.*, Soft-Magnetic Skyrmions Induced by Surface-State Coupling in an Intrinsic Ferromagnetic Topological Insulator Sandwich Structure. Nano Lett. **22**, 881-887 (2022).

[2] T. Fukasawa, S. Kusaka, K. Sumida, *et al*., Absence of ferromagnetism in $MnBi_2Te_4/Bi_2Te_3$ down to 6 K. Phys. Rev. B **103**, 205405 (2021).

[3] Y.-Y. Li, G. Wang, X.-G. Zhu, *et al*., Intrinsic Topological Insulator Bi_2Te_3 Thin Films on Si and Their Thickness Limit. Adv. Mater. **22**, 4002-4007 (2010).

[4] L. Ding, C. Hu, F. Ye, E. Feng, N. Ni, and H. Cao, Crystal and magnetic structure of magnetic topological insulators $MnBi_2Te_4$ and $MnBi_4Te_7$. Phys. Rev. B **101**, 020412(R) (2020).

[5] N. Nagaosa, *et al*., Anomalous Hall effect. Rev. of Mod. Phys. **82**, 1539 (2010).

[6] C.-Z. Chang, *et al*., Thin Films of Magnetically Doped Topological Insulator with Carrier-Independent Long-Range Ferromagnetic Order. Adv. Mater. **25**, 1065 (2013).

[7] X. Kou, *et al*., Interplay between Different Magnetisms in Cr-Doped Topological Insulators. ACS Nano **10**, 9205 (2013).

[8] Y. Gong, *et al.*, Experimental Realization of an Intrinsic Magnetic Topological

Insulator. Chin. Phys. Lett. **36**, 076801 (2019).

[9] Y. Liu, *et al.*, Site Mixing for Engineering Magnetic Topological Insulators. Phys. Rev. X **11**, 021033 (2021).